International Journal of Solids and Structures 259 (2022) 112029

Contents lists available at ScienceDirect

International Journal of Solids and Structures

journal homepage: www.elsevier.com/locate/ijsolstr

On the failure of beam-like topologically interlocked structures

Ioannis Koureas, Mohit Pundir, Shai Feldfogel, David S. Kammer *

Institute for Building Materials, ETH Zurich, Zurich, 8093, Switzerland

ARTICLE INFO

Keywords:
Architectured structures
Frictional contact
Stick-slip governed failure
Saturation level

ABSTRACT

Topologically interlocked structures are architectured by fitting together blocks that are constrained geometrically through contact and friction by their neighboring blocks. As long as the frictional strength is nowhere exceeded, the blocks stick against each other, allowing for large rotations. Once the interfacial stresses exceed the frictional strength, relative sliding between the blocks alters the structure's mechanical response. Improving the structural performance, precisely the strength and the toughness, has been one of the main focal points in the literature. However, many fundamental questions regarding the role and effect of the interface mechanisms (stick and slip) and rotation of the blocks have not been addressed yet. Here, we carry out a parametric analysis to understand the effect of Young's modulus, friction coefficient, and geometry of the blocks on the dominance of the stick or slip-governed mechanism. We combine analytical and computational tools to analyze the failure mechanisms and the response capacities of beam-like topologically interlocked structures. This is achieved using the finite element method coupled with a penalty-based approach for enforcing contact constraints along interfaces. We show that the combination of the structure's height and the friction coefficient controls whether the failure mechanism is slip-governed or stick-governed. Furthermore, we demonstrate that the sticking mechanism across all interfaces along with the rotation of the blocks dictates a saturation level to the mechanical performance of a given structure irrespective of geometric and material properties. This provides a theoretical upper bound for the structural response of topologically interlocked structures and establishes a theoretical benchmark of achievable performance.

1. Introduction

Topologically interlocked structures (TIS) are assemblies of building blocks that hold together due to the blocks' unique interlocking shapes (Dyskin et al., 2001a,b; Djumas et al., 2016; Dyskin et al., 2003a; Schaare et al., 2008). The unbonded nature of the blocks means that TIS rely on contact and frictional interactions between blocks for structural integrity (Fig. 1a). TIS enjoy unique structural properties, including high toughness against failure for structures made from brittle material (Djumas et al., 2016; Mirkhalaf et al., 2014, 2018) and structural integrity despite partial failure (*e.g.*, missing blocks in plate-like TIS) (Dyskin et al., 2003b). However, TIS have not yet found widespread application in engineering because their highly complex, non-linear behavior and failure are not yet fully understood, hindering the ability to design them safely. A better understanding of the behavior and failure of TIS is therefore required and is at the focus of this study.

The main mechanisms governing the behavior and failure of TIS are local slip and stick combined with large block rotations (Mirkhalaf et al., 2018; Khandelwal et al., 2015; Mirkhalaf et al., 2019). These mechanisms take more or less prominent roles in the structural response depending on the TIS design and material properties. However, it remains unclear how these properties determine which mechanism will likely be the more dominant one in a given TIS configuration and how they affect the global structural response in terms of load-carrying capacity, loading energy, global stiffness and ultimate deflection.

In the relatively simple case where the response is entirely stick-governed, the behavior can be described by analytical models as in Khandelwal et al. (2015, 2014, 2012). Khandelwal et al. modeled TIS as a truss and derived analytical expressions for the horizontal and vertical reaction forces F_h and F_v at the local pivoting point A (Fig. 2a), which goes as follows:

$$F_v = F_h\left(\frac{h_{\text{eff}}-\delta}{l_{\text{eff}}}\right) = E\mathcal{A}\frac{l_{\text{eff}}}{\sqrt{l_{\text{eff}}^2+h_{\text{eff}}^2}}\left(\frac{\sqrt{l_{\text{eff}}^2+h_{\text{eff}}^2}}{\sqrt{l_{\text{eff}}^2+(h_{\text{eff}}-\delta)^2}}-1\right)\times\left(\frac{h_{\text{eff}}-\delta}{l_{\text{eff}}}\right) \tag{1}$$

* Corresponding author.
E-mail address: dkammer@ethz.ch (D.S. Kammer).

https://doi.org/10.1016/j.ijsolstr.2022.112029
Received 4 July 2022; Received in revised form 21 September 2022; Accepted 3 November 2022
Available online 8 November 2022

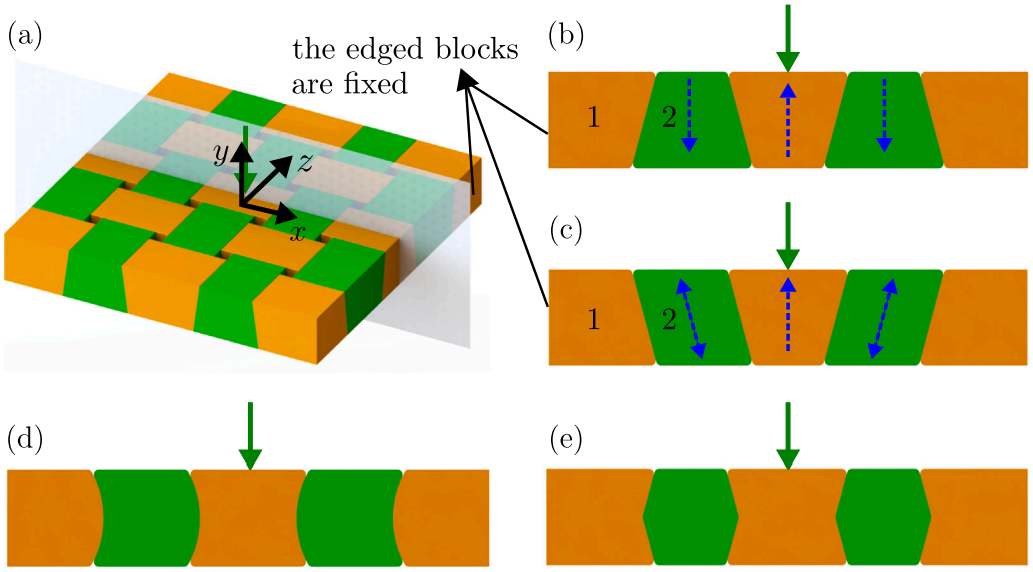

Fig. 1. Rationale for the examined configuration: (a) A topologically interlocked structure (TIS) assembly with planar-faced blocks (Mirkhalaf et al., 2019). (b) Central cross-section in the x–y plane and (c) the basic configuration, which is used for the bulk of this study, is obtained from the original x–y cross-section with the inclination between blocks 1 and 2 flipped. The beam-like structures with (d) curved and (e) kinked surfaces are examined later in relation to Fig. 8 for generality and completeness of the study.

where E is the Young's modulus of the material, h_{eff} and l_{eff} are the effective height and length respectively (Fig. 2), $\mathcal{A}$ is the cross-sectional area of the truss model and δ the applied displacement if no slip occurred so far. Eq. (1) clearly demonstrates that in a sticking situation the load-carrying capacity (*i.e.*, $2F_v$) scales linearly with E and is strongly dependent on h_{eff} and l_{eff}. Although Eq. (1) does not apply when slip occurs, we can still qualitatively explain how local slip reduces global stiffness by examining a specific slipped configuration. Specifically, when slip occurs, the initial pivoting point B moves to B' (Fig. 2b), reducing h_{eff}, F_h and hence the load-carrying capacity $2F_v$. However, these observations remain qualitative, particularly regarding the possible co-existence of stick and slip. Specifically, they do not account for the occurrence of local slips and the consequent evolution of slip-governed failure mechanism. To capture a slip-governed response, which is the most common one in practice and the more challenging one to model, computational methods are required.

The finite element method (FEM) has been shown to capture and quantify the experimentally observed failure and the load–displacement curve in beam-like TIS (Dalaq and Barthelat, 2019; Mahoney and Siegmund, 2022). Dalaq and Barthelat (2019) showed that the failure mode depends on the number of blocks, friction coefficient and the shape of the interfaces, specifically that curved interfaces (a similar configuration is shown in Fig. 1d) promote sliding of the blocks and delay hinging (*i.e.*, stick and rotation) (Dalaq and Barthelat, 2020). However, Dalaq and Barthelat (2020) focused on a specific material and did not investigate the effects of Young's modulus E on the failure mechanisms and the structural capacity. In addition, the effect of the assembly's height h, which governs the bending stiffness of TIS assemblies, see Zakeri et al. (2021), was not considered.

In summary, the effects of h, E and μ on the type of failure, *i.e.*, a slip-governed or stick-governed one and on the associated structural capacities of TIS have hitherto not been addressed in the literature and remain only partially understood. Here, we aim to clarify and quantify these effects. Specifically, we aim to better understand how different combinations of h, E and μ tend to make the response more slip-, or stick-governed and how they affect the structural capacity in terms of maximal load, loading energy, global stiffness and ultimate deflection. Towards that aim, we perform a three-way $E-\mu-h$ parametric study using FEM, based on the latter's ability to capture and quantify experimentally observed failure mechanisms, in particular the slip-governed one, in beam-like TIS (Dalaq and Barthelat, 2019, 2020).

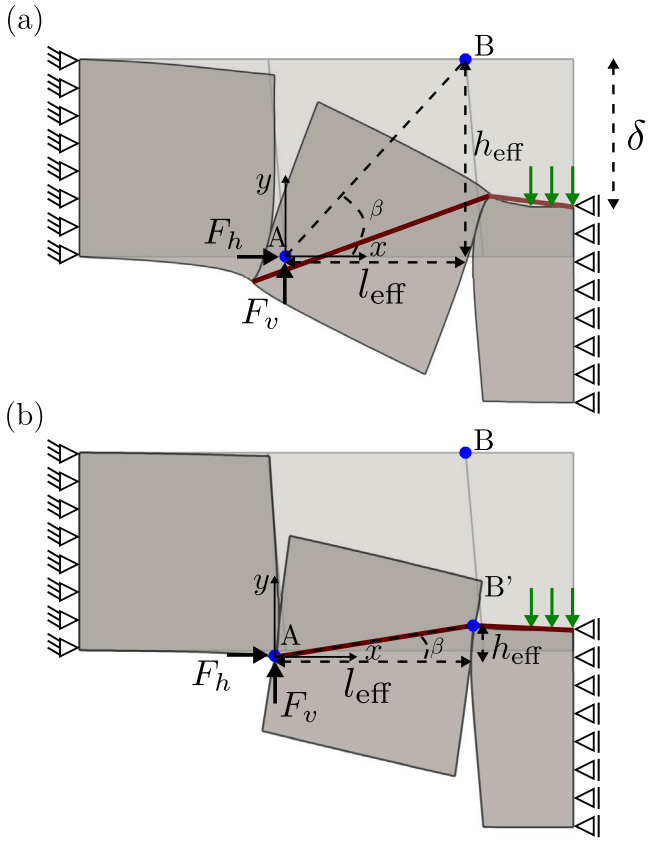

Fig. 2. Equivalent truss model (dark red color) in a topologically interlocked structure (TIS) for (a) a stick and (b) a slip scenario. The effective height h_{eff} and length l_{eff}, as well as the displacement δ are shown for the deformed structures.

In contrast with previous parametric studies that were limited to the stick-regime, the main strength of the present study is that it treats both the stick and the slip regimes within a unified FEM-based framework. This allows us not only to better understand the previously unaddressed

effects of E, μ and h on the slip-governed failure, but also to better understand the conditions that control the two mechanisms.

In the following, we discuss the choice of examined configuration and the FEM formulation (Section 2). In Section 3 we present and discuss the results of the parametric study and give an outlook on how the gained knowledge can aid the design of TIS.

2. Numerical model

2.1. Examined configuration

To address the effects of E, μ and h on the failure and response capacity of TIS, we choose a beam-like configuration inspired by the centrally loaded plate-like planar-faced TIS studied experimentally in Mirkhalaf et al. (2019). The original configuration from Mirkhalaf et al. (2019) is presented in Fig. 1a. The central cross-section of the structure in the x–y plane is depicted in Fig. 1b. The configuration we use for this study is modified compared to the cross-section of the actual 3D TIS such that the angle of inclination of the planar interface between blocks 1 and 2 is reversed, as shown in Fig. 1c.

The concept of simplifying 3D TIS to 2D beam-like structures with a representative cross-section of the 3D equivalent goes back to Khandelwal et al. (2015, 2014, 2012) and Dalaq and Barthelat (2019, 2020). This approach, well-established in structural analysis of monolithic structures, is motivated in the present TIS context by computational and methodological considerations. The computational cost of modeling slip-governed failure in TIS with FEM is always very high and in TIS with more than a few blocks, may be prohibitive (Dalaq and Barthelat, 2020). Methodologically, we assume that the effects of material properties (E and μ) and the structural height (h) on the structural response are qualitatively similar in 3D and 2D TIS, as they are in monolithic counterparts, therefore, we consider the latter. The structural action of beams is much simpler and it allows to study these effects in pure form in accordance with the objectives of the present study.

We note that our configuration is not fully interlocked because there are directions (indicated by blue arrows in Fig. 1b and c) in which the blocks are not kinematically constrained by the neighboring blocks. This scenario is due to the 3D nature of topological interlocking and it is very typical of 2D cross-section representation, like the actual cross-section in Fig. 1b and other beam-like TIS configurations studied in the literature (Khandelwal et al., 2015, 2014, 2012; Dalaq and Barthelat, 2020). To effectively constrain our configuration, we required that (a) the structure has structural integrity under its self-weight and (b) that it is interlocked under the examined loads. Requirement (a) motivated reversing the angle of inclination between blocks 1 and 2 compared to the actual cross-section of the TIS. Requirement (b) is met in our configuration since we only examine a downward load on the central block. By avoiding loads in the few specific directions that are not kinematically constrained (the degrees of freedom in which our configuration deviates from a strictly defined TIS), our configuration may be considered to be effectively TIS under the examined loads. In order to examine the generality of the observation, we consider two additional cases with non-planar interfaces, a curved interface (Fig. 1d) and a kinked interface (Fig. 1e).

2.2. Numerical formulation

FEM is used for the numerical analyses in this study. We employ finite strain formulation to account for the large deformations and large rotations of the building blocks (Bathe et al., 1975). Thus, considering n deformable bodies Ω_n^i, the weak formulation at load increment i is described as:

$$\sum_{\Omega_n^i}^{n} \underline{\underline{\boldsymbol{\varepsilon}}}^i : \mathbb{C} : \delta\underline{\underline{\boldsymbol{\varepsilon}}}^i \, d\Omega_n^i + \sum_{\Omega_n^i}^{n} \underline{\underline{\boldsymbol{S}}}^i : \delta\underline{\underline{\boldsymbol{\eta}}} \, d\Omega_n^i = W_{\text{ext}}^{i+1} - \sum_{\Omega_n^i}^{n} \underline{\underline{\boldsymbol{S}}}^i : \delta\underline{\underline{\boldsymbol{\varepsilon}}} \, d\Omega_n^i \tag{2}$$

Table 1
List of symbols and notations.

Symbol	Description	Unit
E	Young's modulus	N/m^2
F_a	Resultant force at a given pivoting point of the truss model	N
F_y	Load-carrying capacity of the structure	N
$F_{\max}$	Maximum load-carrying capacity of the structure	N
h	Height of a block (= structural depth)	m
h_{eff}	Effective height in a TIS	m
K	*Normalized* global stiffness of the structure	–
l	Length of a block	m
l_{eff}	Effective length in a TIS	m
N	Normal force along a TIS interface	N
t	Thickness of a TIS	m
T	Tangential force along a TIS interface	N
δ	Prescribed displacement at the top central surface of the middle block	m
U	Loading energy of the structure	Nm
β	Angle controlled by h_{eff} and l_{eff}	°
ε_n	Normal penalty parameter	N/m^3
ε_t	Tangential penalty parameter	N/m^3
θ	Inclined angle	°
μ	Friction coefficient	–
μ_{sat}	Saturated friction coefficient	–
ν	Poisson's ratio	–

where, $\underline{\underline{\boldsymbol{S}}}$ and $\underline{\underline{\boldsymbol{\varepsilon}}}$ are the 2nd Piola–Kirchhoff stress tensor and the linear strain tensor, respectively. W_{ext}^{i+1} is the virtual work of the external forces, $\underline{\underline{\boldsymbol{\eta}}}$ represents the nonlinear incremental strain tensor and $\mathbb{C}$ the 4th order constitutive tensor. A node-to-segment contact algorithm, with penalty-based constraints, is employed (Konyukhov and Schweizerhof, 2004; Schweizerhof and Konyukhov, 2005; Laursen, 2003; Wriggers and Laursen, 2007; Yastrebov and Breitkopf, 2013; Zavarise and De Lorenzis, 2009b) to enforce contact and frictional constraints along the interfaces of n deformable bodies. We use the penalty method for its computational simplicity. The virtual work δW_c of the contact forces at the current configuration for n deformable bodies that come in contact at k interfaces S_k is expressed as:

$$\delta W_c = \sum^{k} \int_{S_{k_{\text{slave}}}} (T_n \boldsymbol{n} + \boldsymbol{T}_t) \cdot (\delta \boldsymbol{u}_{k_{\text{slave}}} - \delta \boldsymbol{u}_{k_{\text{master}}}) \, dS_{k_{\text{slave}}} \tag{3}$$

where T_n is the traction along the normal $\boldsymbol{n}$ to the interface and $\boldsymbol{T}_t$ is the frictional traction tangential to $\boldsymbol{n}$ integrated over one of the two contact surfaces termed as slave surface. Based on the penalty approach, $T_n = \varepsilon_n \langle g \rangle$ is approximated as a linear function of the orthonormal gap between a slave node and the master surface. Similarly, $\boldsymbol{T}_t = \varepsilon_t(\boldsymbol{\Delta u}_t)$ is approximated as a linear function of the tangential slip distance $(\boldsymbol{\Delta u}_t)$ between a slave node and the master surface, computed based on the covariant derivative approach (Schweizerhof and Konyukhov, 2005; Wriggers et al., 2001). The penalty parameters $(\varepsilon_n, \varepsilon_t)$ are area regularized to ensure that the computed contact forces are mesh independent (El-Abbasi and Bathe, 2001; Zavarise and De Lorenzis, 2009a). In order to overcome the biases in choosing a slave and master surface at an interface (see Eq. (3)), a two-pass algorithm (El-Abbasi and Bathe, 2001; Zavarise and De Lorenzis, 2009a) is employed whereby at each load increment, the contact forces at a node are computed considering once a surface as a slave and then as a master. The FE code with the finite strain formulation and the node-to-segment contact algorithm, is developed as in-house code and has been validated for frictional cases (more details provided in Appendix A.1).

The examined structure is depicted in Fig. 3a. We consider a five-block assembly with a span length of 10 mm and three different heights (h = 1 mm, h = 1.5 mm and h = 2 mm). It is fixed at its ends (*i.e.*, $u_y(\pm 5, y) = u_x(\pm 5, y) = 0$) and it is loaded incrementally by prescribing the displacement $u_y(-0.25 \le x \le 0.25, h/2) = \delta = h/500$. The total force corresponding to δ is denoted by F_y. Using the symmetry about the y-axis, we model only the left half of the structure, where the symmetry boundary condition $u_x = 0$ is prescribed along $x = 0$.

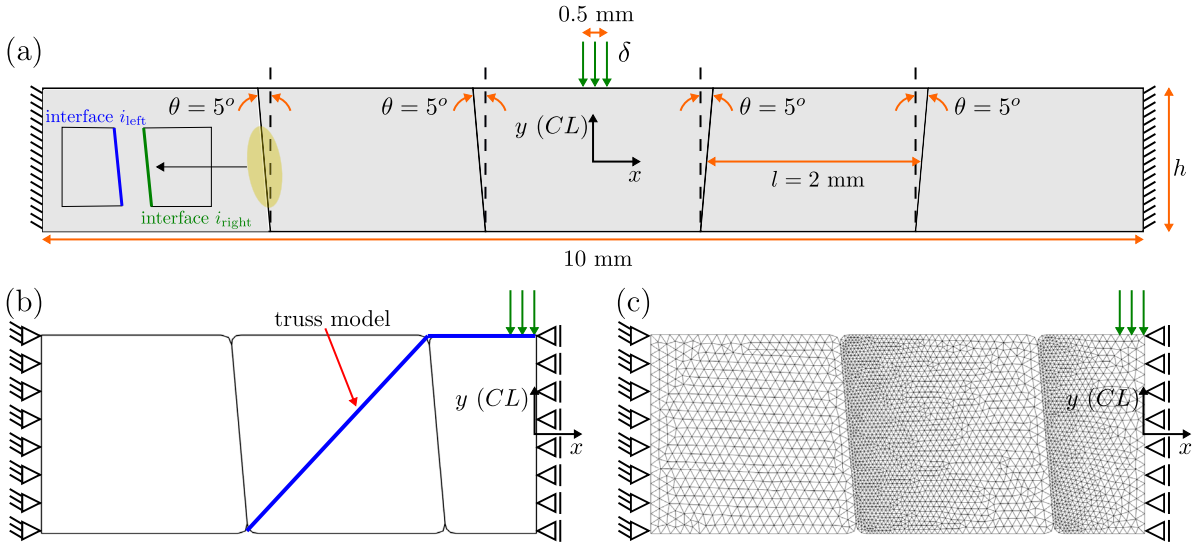

Fig. 3. Schematic representation of model set-up showing (a) the geometric parameters and boundary conditions in a five-block topologically interlocked structure (TIS). Every structure consists of i interfaces where $i = 1, 2, \ldots, k$ with k being the total number of interfaces in a structure. Every interface consists of two sides, the left and the right. (b) Schematic illustration of the symmetric model with respect to the center line (CL). The blue line represents the truss model. (c) Mesh and boundary conditions as used in the simulation.

Table 2
Material and geometrical parameters.

Parameter	Value
E (GPa)	1, 2, 3, 10, 20, 30
h (mm)	1.0, 1.5, 2.0
l (mm)	2.0
t (mm)	1.0
θ (°)	5
μ	0.2, 0.4, 0.6, 0.8, 1.0, 1.2
ν	0.2

Each block is characterized by its angle θ, height h and length l. The blocks are considered to be isotropic linear elastic material with Young's modulus E, Poisson's ratio ν and friction coefficient μ. A description of the symbol notation we use is provided in Table 1. The material and geometrical values used for the parametric analyses are presented in Table 2. We chose values of E that cover an essential range of brittle materials and allow us to study the effect of material elasticity on the global stiffness of TIS. Furthermore, we explore a wide range of μ to understand the effect of interfacial friction of the blocks. The effects of fracture are not accounted.

For the numerical analysis, the topologically interlocked beam (Fig. 3b) is modeled as a 2D structure under plane-strain conditions. The structure is discretized using first-order triangular elements (Fig. 3c) and the corners are rounded to avoid non-physical stress singularities. All simulations are performed under static conditions. Therefore, dynamic effects of friction and inertial effects that may be associated with the structural response are not considered.

To validate our FE formulation in the context of TIS, we analyzed the five-block pre-compressed assembly studied in Dalaq and Barthelat (2019). The results show that the model compares well, both qualitatively and quantitatively with the analytical model and reasonably well with the experiments (Fig. 4), supporting the validity of our approach.

A sensitivity analysis based on the global load response and the local interface mechanism is performed (see Appendix A.2). We chose mesh refinement and the penalty parameters such that both converged.

3. Results and discussion

3.1. Global response

In our analysis we explore the effects of h, E and μ on the slip and stick-governed failure mechanisms and on the global response.

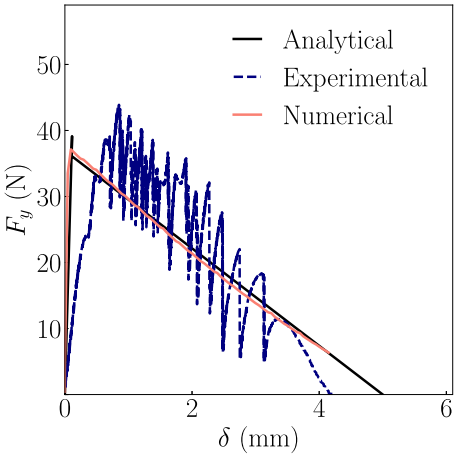

Fig. 4. Load-carrying capacity F_y against the prescribed displacement δ for a five-block pre-compressed structure with angle $\theta = 0°$. The experimental and analytical results have been taken from Dalaq and Barthelat (2019).

Specifically, the maximum load-carrying capacity (F_{max}), loading energy (U), global normalized stiffness (K) and ultimate deflection. F_{max} is computed as the maximum value of F_y and the loading energy as $U = \int_0^{\delta_{max}} \boldsymbol{F}(\delta) d\delta$ with δ_{max} such that $\boldsymbol{F}(\delta_{max}) = 0$ and $\frac{\partial \boldsymbol{F}}{\partial \delta}\Big|_{\delta_{max}} < 0$. K is defined by the secant slope in the $F_y - \delta$ curves at $\delta/h = 0.05$ (Fig. 5a). Since fracture is neglected, the failure of the structure is characterized by the central block being completely pushed out of the structure. The relation between F_{max}, U, K and ultimate deflection is investigated for the different structures with a focus on the underlying mechanisms causing these properties.

Fig. 5 depicts the normalized $F_y - \delta$ curves for all values of h, μ and E examined. F_y is normalized with respect to h, t and E while the deflection is normalized with respect to h to remove the scalability effect. In all cases, there is a non-monotonic behavior. The force initially increases linearly with the prescribed displacement. It gradually deviates from the linear behavior and eventually reaches a peak value F_{max}. Beyond that point, the force decreases until it reaches zero similar to other studies (Mirkhalaf et al., 2019; Khandelwal et al., 2012).

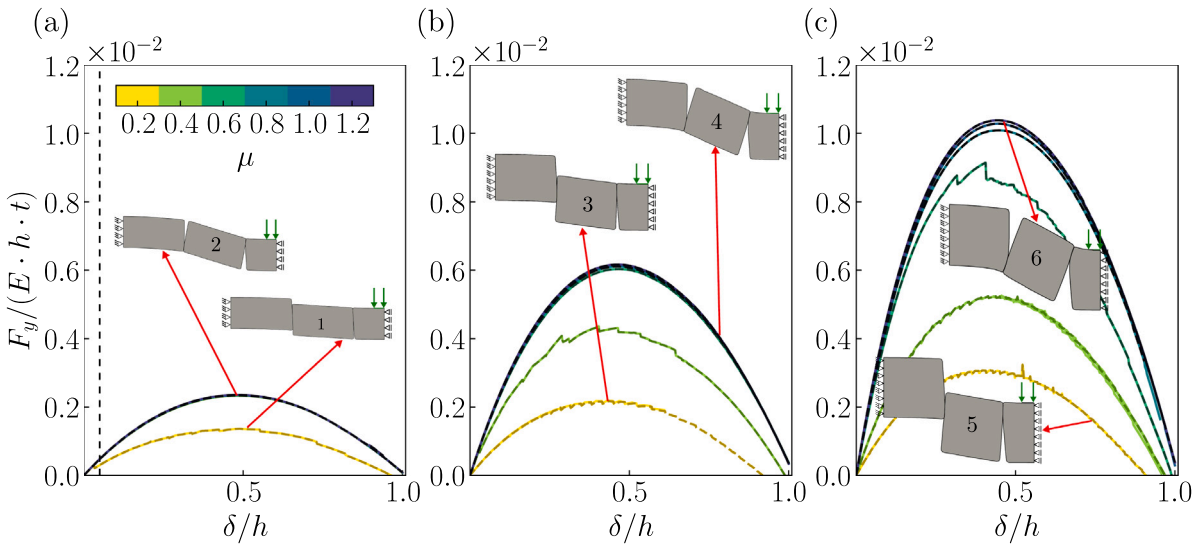

Fig. 5. Load-carrying capacity F_y normalized with respect to the Young's modulus E, the height h and thickness t of the structure against the prescribed displacement δ normalized with respect to h. The curves correspond to a structure with angle $\theta = 5°$ with (a) $h = 1.0$ mm, (b) $h = 1.5$ mm and (c) $h = 2.0$ mm. The structures numbered 1, 3 and 5 show cases where the slip mechanism is observed while structures 2, 4 and 6 show cases where the stick mechanism is observed. The dashed lines on the normalized $F_y - \delta$ curves represent the lowest value of E (1 GPa). Each curve is an overlap of six curves that correspond to the different values of E. The dashed vertical black line represents $\frac{\delta}{h} = 0.05$ which is used to compute the global stiffness K.

Effect of μ

Fig. 5 shows that, for each of the examined h's, the curves with the lowest F_{max} are associated with the smallest μ's indicated by yellow lines. The associated mechanism in these cases, represented by snapshots 1, 3 and 5, involves slip along the interfaces. In contrast, the curves with the highest F_{max} are associated with the highest μ's and the associated mechanisms, represented by snapshots 2, 4 and 6, are entirely stick-governed. These observations mean that higher μ is conducive to increasing the structural capacity insofar as it promotes sticking mechanisms.

Fig. 6 depicts the direct dependence of F_{max}, as well as U and K, on μ, for all examined beam heights (indicated by different markers). All three response parameters initially increase as a function of μ, but later saturate at higher values of μ (shown by the shaded regions in Fig. 6). The saturation of all three response parameters is reached at effectively the same μ, denoted by μ_{sat}. The μ_{sat} for $h = 1$, 1.5 and 2 mm are 0.4, 0.6 and 0.8, respectively, as indicated in Fig. 6.

To address the effects of spatial variability of μ along the interfaces, we consider the case where μ is randomly chosen from a normal distribution with mean 0.6 and a standard deviation of 0.4 (with $h =$ 2 mm). Fig. 7 depicts $F_y - \delta$ from 50 random realizations, indicated in light yellow. While μ varied within 66% of the mean, F_{max} varied within only 20% of the average value, indicated by the green dashed line and it is close to the response without μ variability, indicated by the blue dashed line. This suggests that the effect of spatial variability of μ is relatively mild. Also, even the realizations with the highest F_{max} do not exceed the saturated response ($\mu_{sat} = 0.8$) corresponding the same geometry, shown by the black dashed line. This shows that having higher-than-saturated μ's along the interface can never lead to higher F_{max} than the saturated one.

Effect of h

$F_{\max}$, U and K increase as a function of h (Fig. 6). In addition, Fig. 5 shows that while h increase, more $F_y - \delta$ curves lie below the saturated curves. These curves are characterized by sliding mechanism. For example for $h = 1$ mm sliding occurs only for $\mu = 0.2$ (Fig. 5a structure 1). For $h = 1.5$ mm sliding occurs when $\mu = 0.2$ (Fig. 5b structure 3) and $\mu = 0.4$. Finally, for $h = 2$ mm sliding occurs when $\mu = 0.2$ (Fig. 5c structure 5), 0.4 and 0.6. For a constant μ, as h increases, the magnitude and the direction of the thrust line changes, which alters the normal and tangential forces at the contact points. Based on Coulomb friction, a point is reached where the ratio between the tangential and normal forces exceeds the friction coefficient and the structure starts sliding. Based on the results, but also from analytical expressions derived in the literature (Khandelwal et al., 2014; Dalaq and Barthelat, 2019), we find $K \propto h$. The smaller the h, the smaller the compression experienced by TIS and, therefore, the smaller the $F_{\max}$, U and K. We therefore conclude that the increase of h promotes sliding.

The ultimate deflection in a beam-like TIS in our study never exceeds the structure's height (h). This is in agreement with the analytical expression from Eq. (1). When the applied displacement becomes equal to the structure's height, the reaction force becomes zero showing that the maximum deflection is equal to h. Therefore, μ, h and E are the main parameters that affect the global response of TIS and ultimately $F_{\max}$, U, K and ultimate deflection.

Effect of E

In Fig. 5, the $F_y - \delta$ curves are normalized by E. We found that, for each h and μ (*e.g.*, the yellow curve in (Fig. 5a) corresponding to $h = 1$ mm and $\mu = 0.2$), the normalized curves to the six examined E are identical. This exact linear scaling with E suggests that the response is qualitatively identical in the six cases and that E only affects the magnitude of the response parameters (irrespective of μ and h), but not the mechanisms (as we indeed show later in Section 3.2). The presence of a linear relationship between E and mechanical response for such a wide range of friction coefficients is a new observation. Such a linear dependency can be predicted for high values of μ, assuming that slipping is suppressed along the interfaces (see Eq. (1) and Khandelwal et al. (2014)). However, for lower values of friction coefficient ($\mu = 0.2, 0.4$), where the slipping occurs, such a linear dependency has not been shown.

Effect of interface geometry

Our work shows that the described beam-like structures reach theoretical maximum response capacities with μ_{sat} independently on the

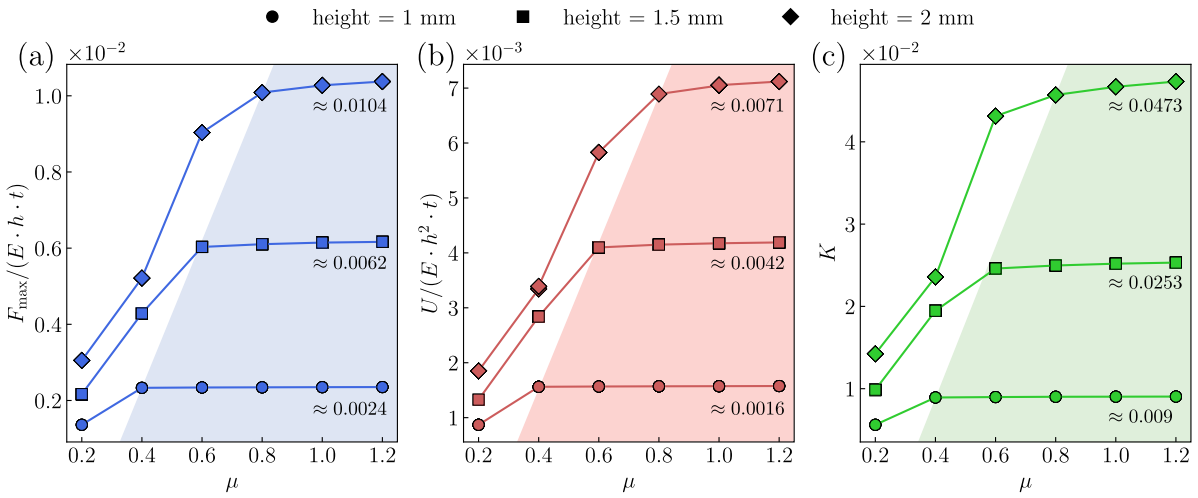

Fig. 6. Overview of the mechanical performance of beam-like TIS, showing the saturation for (a) the maximum load-carrying capacity F_{max}, (b) the loading energy U normalized with respect to the Young's modulus E, the height h and thickness t of the structure and (c) the normalized global stiffness K plotted against the friction coefficient μ for structures with $h = 1.0$ mm, $h = 1.5$ mm and $h = 2.0$ mm. By increasing μ the structure reaches a maximum value for all cases (see the approximated value). The lines have been added as a visual aid. The shaded areas signify the saturated regions.

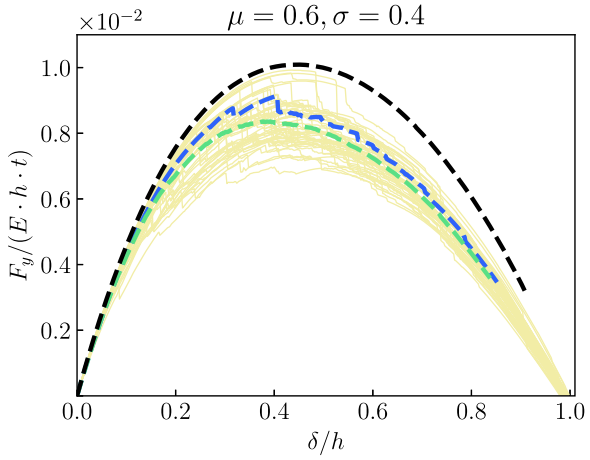

Fig. 7. Effect of μ variation along a interface. Load-carrying capacity F_y normalized with respect to the Young's modulus E, the height h and thickness t of the structure against the prescribed displacement δ normalized with respect to h for $\mu = 0.6, \sigma = 0.4$. 50 simulations were ran for each case, shown by the light yellow curves. The average load response of 50 simulations is shown by green dashed curve. For comparison, we also show the load responses for the cases where $\mu = 0.6$ is constant along the interface, (shown in dashed blue curve) and where $\mu = \mu_{sat} = 0.8$ is constant along the interface (shown in black dashed curve).

material properties (E) and geometrical parameters (h, l). This observation was obtained based on the behavior of blocks with planar interfaces. To further generalize our observation we consider two additional structures (with $h = 2$ mm). The first one is a five-block structure with curved interfaces and curvature ratio $c = l/R = 1$. Here R is the radius of the curvature. The second is a five-block structure with kinked interfaces and inclined angle $\theta = 5°$. The capacity saturation curves and a snapshot of the failure mechanism are shown for the two cases in Fig. 8c and d. Like the blocks with planar interfaces, the load-carrying capacity attains saturation. However, for structures with curved interfaces, the saturation level required a greater μ (*i.e.*, $\mu_{sat} = 2$) compared to the cases with straight interfaces (*i.e.*, $\mu_{sat} = 0.8$ and $h = 2$ mm). This observation is in agreement with Dalaq and Barthelat (2019), who showed that curved surfaces can promote sliding mechanism and delay sticking. Finally, we note that the use of curved surfaces reduces the value of the saturation level (*i.e.*, $F_{max}/(E \cdot h \cdot t) \approx 0.008$) compared to ($F_{max}/(E \cdot h \cdot t) \approx 0.01$) for the planar interfaces. In addition, sliding does not allow the structure to reach the maximum theoretical deflection.

3.2. The type of failure mechanism

The nature of TIS suggests that their mechanical performance is the direct result of interfacial mechanisms. To better understand the effect of TIS mechanisms on the mechanical behavior of the structure we deemed necessary to take a closer look at the interface between the blocks. We now consider which combinations of h and μ lead to a stick-governed failure and which lead to a slip-governed one. We also verify that E does not affect the interface mechanism, as discussed in the previous section.

Stick and slip can be defined per a given load increment and per the entire response, the latter being the definitive one for our discussion. Per a given increment, we distinguish between the node level, the interface level and the structure level. The node level is binary - a node sticks when the tangential traction is smaller than the tangential capacity and slips otherwise. At the interface level, we define the slipping percentage to be the percentage of nodes that slip and we consider an interface to stick when at least one node sticks, that is when the slipping percentage is less than 100%. The structural level is also binary - a structure is sticking if and only if all the interfaces are sticking and sliding otherwise.

At the level of the entire response, we also consider the distinction between stick and slip to be binary — the response is stick-governed if and only if the structure sticks in all load increments and slip-governed otherwise.

Fig. 9 illustrates these definitions for $h = 2$ mm, $\mu = 0.6$ and all examined E. Fig. 9a shows the evolution of sliding percentage in both interfaces throughout the response. The overall mechanism does not change by changing E. Fig. 9b indicates interfaces 1 and 2 and shows snap shots of the deformed structure at $\delta/h = 0.15$ and at 0.35. Fig. 9a shows that interface 1 is slipping up to about $\delta/h = 0.25$ (sliding percentage = 100%) and alternately sticks and slips thereafter. Interface 2 is sticking throughout (sliding percentage < 100%). From the fact that there are load increments with 100% percent sliding, we conclude that the response in this case is slip-governed.

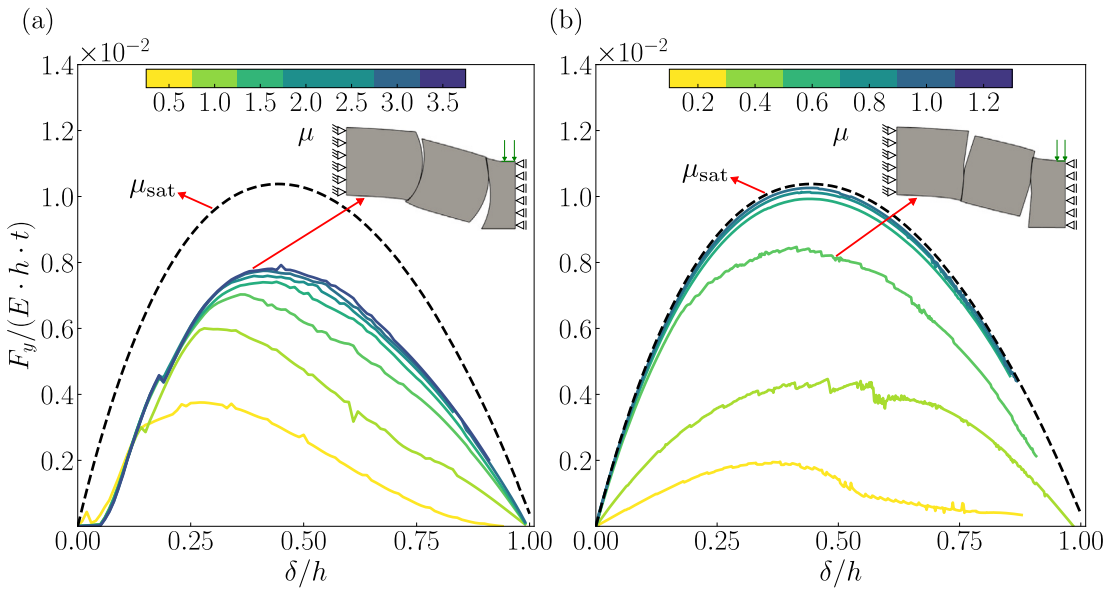

Fig. 8. Load-carrying capacity F_y normalized with respect to the Young's modulus E, the height h and thickness t of the structure against the prescribed displacement δ/h. The curves correspond to (a) a five-block structure with curved interfaces and curvature ratio $c = l/R = 1$ with R being the radius of the curvature and (b) a five-block structure with kinked interfaces and angle $\theta = 5°$. The black dashed line corresponds to the equivalent saturated curve for five-block structure with planar interfaces and $\mu = 1.2$.

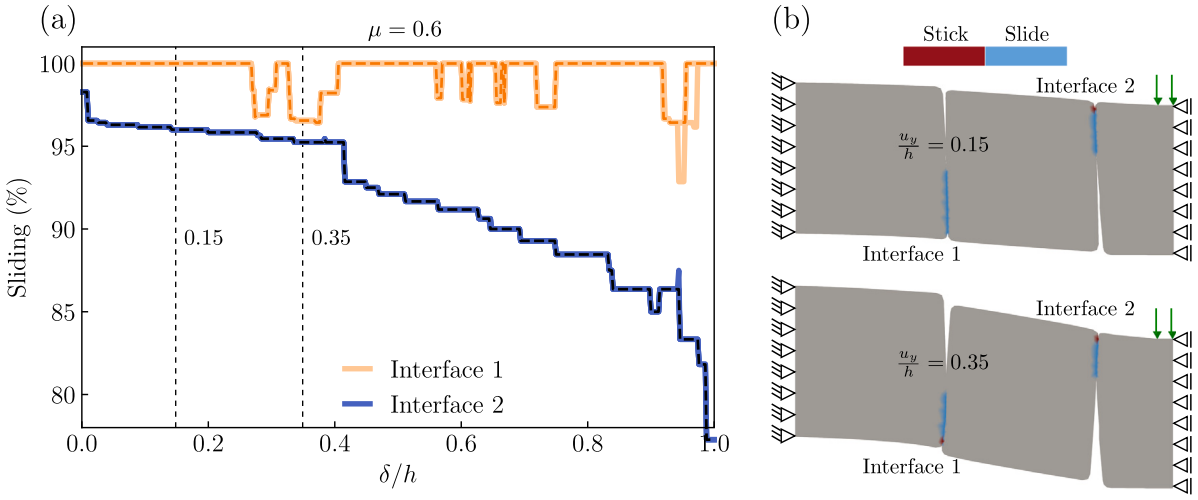

Fig. 9. Interface mechanism. (a) Percentage of sliding against the prescribed displacement δ/h at every interface of a structure with height $h = 2$ mm and $\mu = 0.6$. (b) Snapshots capturing the sliding and sticking mechanisms at the interfaces of the structure at $\delta/h = 0.15$ and $\delta/h = 0.35$. The colored dashed lines represent the sliding percentage for $E = 1$ GPa.

Based on the above definitions, Fig. 10 depicts the type of failure as a function of μ and h with red and blue circles indicating slip- and stick-governed responses, respectively. In addition to the results of our analyses, Fig. 10 also includes an analytically derived line based on Khandelwal et al. (2014) which parses the parameter space to stick- and slip-governed regions (see Appendix A.3 for the derivation of the analytical line). Fig. 10 shows that the higher the h is, the response is slip-governed for higher μ. This quantitatively supports the previous observation that higher h promote sliding. The fact that the response is slip-governed for most of the realistic range of μ between 0.2–0.4 reflects the larger prevalence of this mechanism observed in experiments, which designates this regime as the one of more practical relevance. This underlines the importance and relevance of accounting for the effects of E, μ and h specifically in the slip-governed context, which is at the focus of the present research. Lastly, the fact that the analytically derived line is in close agreement with our results supports the validity of our modeling approach.

3.3. Saturated friction coefficient from a design perspective

In all cases examined, the saturation level has been reached for high μ_{sat} for common building materials. This raises a question regarding the practical relevance of capacity saturation. Nevertheless, recalling that what defines capacity saturation is the condition of no-slip and that high μ_{sat} is but one way of obtaining this condition, capacity saturation is actually relevant in systems where slips are suppressed by means other than high μ_{sat}. One example of increasing the effective surface resistance to sliding is through architectured surfaces, or surface-level-interlocking, see Djumas et al. (2017). In such systems, the high μ_{sat} can be viewed as an approximate measure of the (geometrically-induced) macroscopic surface resistance to sliding. Considering μ as a generalized measure of effective sliding resistance, the phenomenon of capacity saturation is realistic and relevant in all systems where this resistance can be increased to the point of suppressing sliding completely, regardless of the actual friction coefficient.

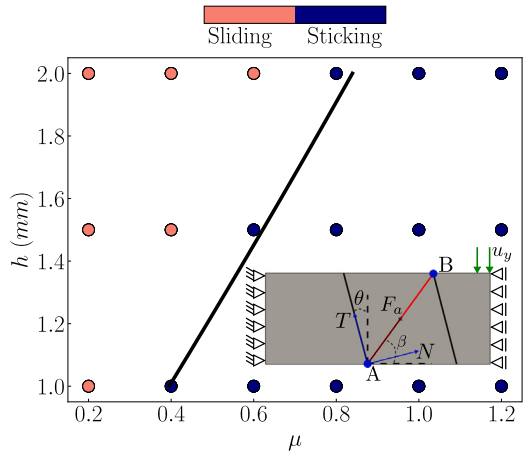

Fig. 10. Global failure mechanism. Dark points correspond to setups that lead to failure governed by sticking, whereas light points correspond to setups that lead to slip-governed failure. The black line represents the boundary based on the analytical solution from the truss model (Eq. (A.6)).

3.4. General comments

The sliding and rotation of the blocks are crucial for the mechanical behavior of TIS as it introduces a non-linear behavior in a structure made from a linear elastic material. When sticking occurs, applied work is stored in the form of elastic energy (Djumas et al., 2017; Krause et al., 2012). In that case, K is controlled by E of the blocks, l_{eff} and h_{eff}. The structure can be described as elastic when the model is characterized by the stick and rotation mechanisms. As a result, the model is load-independent. When sliding occurs, however, the structure becomes load-path dependent. The advantage of such a structure is that the building blocks do not physically undergo plastic deformation but only the structure. Moreover, it is possible to have a structure that initially sticks (behaves elastically) within the service range. However, it can also behave inelastically (through sliding) once it exceeds a specific value. Design parameters alongside material properties are considered the main factors affecting the ultimate behavior of TIS. Therefore, we conclude that TIS made from linear elastic materials can express both elastic and inelastic behavior at the structural scale.

4. Conclusion

This study presented a parametric analysis of TIS to understand how the elastic modulus E, the friction coefficient μ and the structural height h affect the interfacial failure mechanisms and the response capacity of beam-like topologically interlocked structures. From this parametric analysis, we can conclude that as μ increases, the response is more stick-governed and the response parameters increase with h and (linearly) with E. For all examined block geometries and given E and h, there always exists a saturation level of the structural capacity as a function μ. In addition, for relatively small values of μ, sliding occurs at interfaces, decreasing the effective height of the structure, which in turn leads to a decrease in the load-carrying capacity. Finally, h and E of the blocks mainly control the structure's response capacity while μ and the interface geometry control the type of mechanism (stick or slip) that governs the failure. Specifically, the response parameters scale linearly with E not only in the stick mechanism (as observed previously) but also in the more commonly observed slip mechanism. Alongside the observation of capacity saturation with increasing μ, the two main and original, contributions of this study are: (a) that it addresses the effects of E, μ and h on the slip-governed failure of TIS; and (b) that it elucidates the conditions that govern the occurrence of the stick or the slip mechanisms. The insights and observations from this study, particularly the phenomenon of capacity saturation, are relevant from a design perspective and they will serve as the starting point for future work.

Declaration of competing interest

The authors declare that they have no known competing financial interests or personal relationships that could have appeared to influence the work reported in this paper.

Data availability

The simulation data generated in this study have been deposited in the ETH Research Collection database

Acknowledgments

We acknowledge Dr. Vladislav Yastrebov, MINES ParisTech for the helpful discussions.

Appendix

A.1. Validation of frictional contact

Since the behavior and failure of TIS completely depends on friction resistance and stick and slip mechanisms, the accuracy of the results depend entirely on the validity of the contact formulation. As further validation of the frictional contact, the Cattaneo and Mindlin's problem is considered. This benchmark involves two elastic cylinders that are pressed together. The bottom half-cylinder has its base constrained in the vertical and horizontal direction while the top surface of the top half cylinder is displaced by δ_x and δ_y (Fig. A.11a). The normal T_n and tangential T_t tractions along the contact surface are computed and plotted together with the analytical solution. For computing the analytical solution, the normal F_n and tangential F_t reaction forces are calculated from the surface where the prescribed displacement is applied. Using the analytical solution (Barber, 2010) T_n and T_t are computed as:

$$T_n(x) = \frac{2F_n\sqrt{\alpha^2 - x^2}}{\pi\alpha^2} \tag{A.1}$$

$$T_t(x) = \frac{2\mu_s F_n}{\pi\alpha^2}\left[\sqrt{a^2 - x^2} - H(c^2 - x^2)\sqrt{c^2 - x^2}\right], \quad -\alpha < x < \alpha \tag{A.2}$$

where,

$$\alpha = \left[\frac{4F_n R_0 R_1}{\pi(R_0 + R_1)}\left(\frac{1-\nu_0^2}{E_0} + \frac{1-\nu_1^2}{E_1}\right)\right]^{\frac{1}{2}} \text{ and } \quad c = \alpha\left(1 - \frac{F_t}{\mu_s F_n}\right)^{\frac{1}{2}} \tag{A.3}$$

Here, $H(\cdot)$ denotes the Heaviside function. A friction coefficient $\mu_s = 0.5$ is used and penalty parameters $\varepsilon_n = \varepsilon_t = 10^{12}$ N/m^3. The numerical results of T_t (Fig. A.11b) and T_n (Fig. A.11c) are in good agreement with the results from the analytical solution.

A.2. Convergence analysis

For the mesh density analysis, a five-block structure is used, with $\theta = 5°$, $E = 30$ GPa, $h = l = 2$ mm and $\mu = 0.2$ and 1.2. We chose two different μ to ensure that the interface behavior (slip or stick) does not influence the chosen mesh density. The particular mesh design is purely chosen based on computational efficiency. Having a similar fine mesh density everywhere in the domain increases the computational time of the simulation. We ran simulations with same mesh density everywhere and compared the $F_y - \delta$ curves for the case where densities are different (Fig. A.12). As can be observed the behavior difference in mesh densities around an interface does not affect the global response behavior. Fig. A.12a shows the chosen mesh density for the planar-faced interfaces and Fig. A.12c shows the chosen mesh densities for the curved and kinked interfaces.

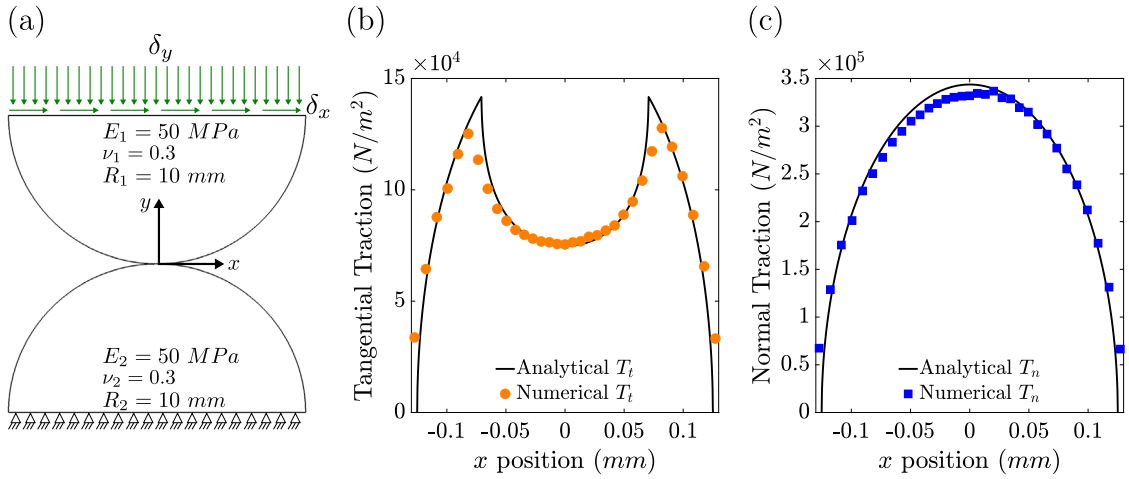

Fig. A.11. Benchmark with the Cattaneo and Mindlin's problem. (a) Schematic setup showing the geometry of the half-cylinders, the boundary conditions applied and the material properties used in the simulation. Distribution of (b) T_t and (c) T_n as computed numerically (circles and squares respectively) and in comparison with the analytical solution (solid black lines) for friction coefficient $\mu_s = 0.5$.

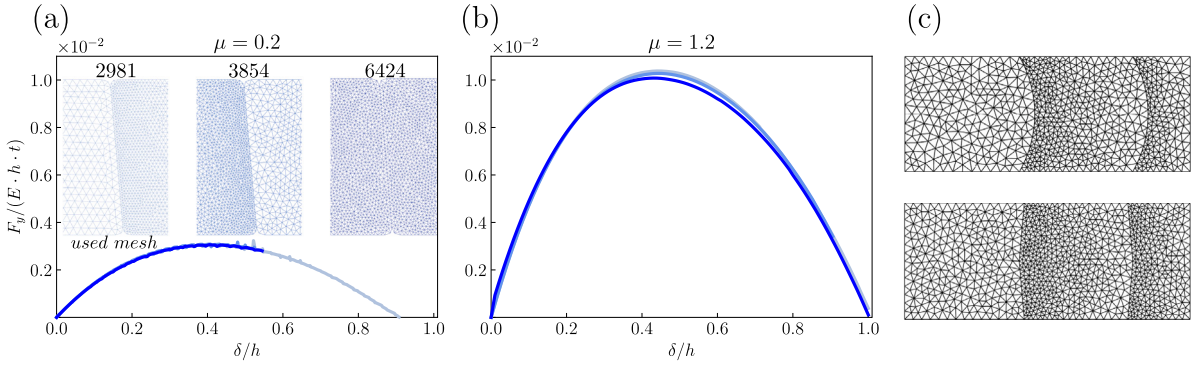

Fig. A.12. Mesh density convergence analysis. Load-carrying capacity $F_y/(E \cdot h \cdot t)$ against the prescribed displacement δ/h for (a) $\mu = 0.2$ and (b) $\mu = 1.2$. The number of nodes is shown for each examined mesh density. (c) Mesh density for the curved (top) and kinked (bottom) configurations.

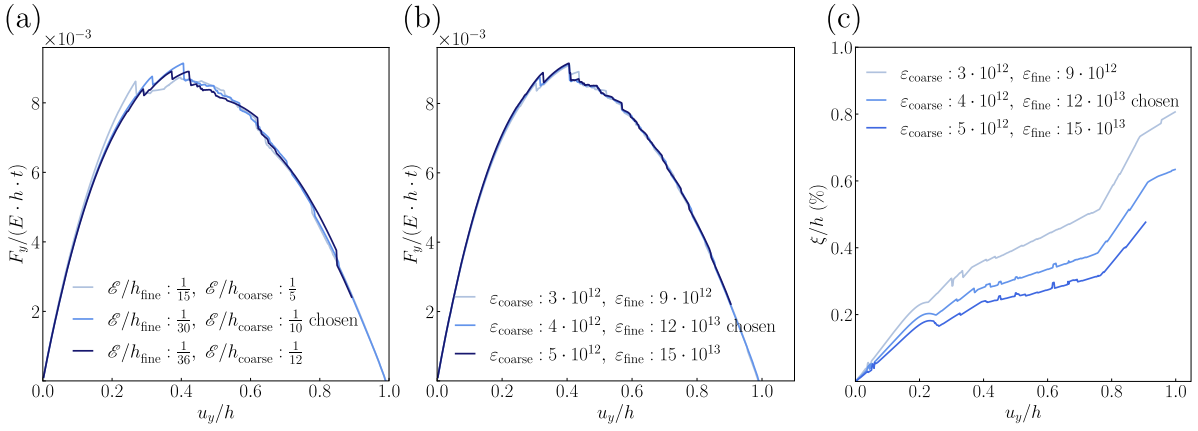

Fig. A.13. Convergence analysis. Load-carrying capacity $F_y/(E \cdot h \cdot t)$ against the prescribed displacement δ/h. The curves correspond to (a) different mesh densities (where the mesh density is chosen based on the ratio between the element size $\mathscr{E}$ and h of the structure) and (b) different penalty parameters. (c) The chosen penalty parameters are tested to ensure that the ratio between the penetration ξ and h (*i.e.*, ξ/h) < 1%.

In addition, the chosen mesh from the mesh density analysis (Fig. A.12) is used for the convergence analysis. A five-block structure is used, with $\theta = 5°$, $E = 1$ GPa, $h = l = 2$ mm and $\mu = 0.6$. The $F_y - \delta$ response is examined for different mesh refinements (Fig. A.13a). The mesh size along the fine and coarse interfaces is chosen based on the ratio between the element size $\mathscr{E}$ and the height h of the structure. The rest of the structure has mesh density equal to the coarse mesh. The results from the $F_y - \delta$ curves are very similar and independent of the chosen mesh refinements. The chosen mesh is based on the fact that a sufficient number of nodes at the interface is needed to properly capture stick and slip mechanisms, but also to ensure reasonable computational cost. The chosen mesh is then tested for different penalty parameters ε_n and ε_t (Fig. A.13b). The chosen penalty parameters do not affect the $F_y - \delta$ response. Moreover, we tested that the penetration ξ of a slave

node is small enough such that $\xi/h < 1\%$ (Fig. A.13c). Finally, ϵ_n and ϵ_t are kept constant at a given surface.

A.3. Derivation of analytical expression for stick–slip threshold

The results are compared with an analytical line derived from the truss model (Eq. (1)) marking the boundary between the stick- and slip-governed regions. We derive a theoretical boundary that marks the global transition from sticking to a slipping regime by employing the truss model for TIS, as discussed in Khandelwal et al. (2014) and Coulomb's friction law ($T = \mu N$). The tangential force T and the normal force N along an interface of TIS are computed by resolving F_v and F_h into F_a along a respective direction (β) as follows:

$$N = -\left(\Big(sin(\beta)sin(\theta) + cos(\beta)cos(\theta)\Big)F_a\right) \tag{A.4}$$

$$T = -\left(\Big(sin(\beta)cos(\theta) - cos(\beta)sin(\theta)\Big)F_a\right) \tag{A.5}$$

Angle β is controlled by h_{eff} and l_{eff} (Fig. 2). The expressions from (A.4) and (A.5) are substituted into the Coulomb friction model for computing μ_{sat} that controls the transition from sliding to global sticking:

$$T = \mu_{\text{sat}} N \implies \mu_{\text{sat}} = \frac{sin(\beta)cos(\theta) - cos(\beta)sin(\theta)}{sin(\beta)sin(\theta) + cos(\beta)cos(\theta)} \tag{A.6}$$

References

Barber, J.R., 2010. Elasticity, 172 of Solid Mechanics and Its Applications. Springer Netherlands, Dordrecht, http://dx.doi.org/10.1007/978-90-481-3809-8.

Bathe, K.-J., Ramm, E., Wilson, E.L., 1975. Finite element formulations for large deformation dynamic analysis. Internat. J. Numer. Methods Engrg. 9 (2), 353–386. http://dx.doi.org/10.1002/nme.1620090207, 1975.

Dalaq, A.S., Barthelat, F., 2019. Strength and stability in architectured spine-like segmented structures. Int. J. Solids Struct. 171, 146–157. http://dx.doi.org/10.1016/j.ijsolstr.2019.04.012, Elsevier Ltd, 2019.

Dalaq, A.S., Barthelat, F., 2020. Manipulating the geometry of architectured beams for maximum toughness and strength. Mater. Des. 194, 108889. http://dx.doi.org/10.1016/j.matdes.2020.108889, Elsevier Ltd, 2020.

Djumas, L., Molotnikov, A., Simon, G.P., Estrin, Y., 2016. Enhanced mechanical performance of bio-inspired hybrid structures utilising topological interlocking geometry. Sci. Rep. 6 (January), 1–10. http://dx.doi.org/10.1038/srep26706, Nature Publishing Group, 2016.

Djumas, L., Simon, G.P., Estrin, Y., Molotnikov, A., 2017. Deformation mechanics of non-planar topologically interlocked assemblies with structural hierarchy and varying geometry. Sci. Rep. 7 (1), 11844. http://dx.doi.org/10.1038/s41598-017-12147-3, Springer US, 2017.

Dyskin, A.V., Estrin, Y., Kanel-Belov, A.J., Pasternak, E., 2001a. A new concept in design of materials and structures: Assemblies of interlocked tetrahedron-shaped elements. Scr. Mater. 44 (12), 2689–2694. http://dx.doi.org/10.1016/S1359-6462(01)00968-X, 2001.

Dyskin, A.V., Estrin, Y., Kanel-Belov, A.J., Pasternak, E., 2001b. Toughening by fragmentation-how topology helps. Adv. Eng. Mater. 3 (11), 885–888. http://dx.doi.org/10.1002/1527-2648(200111)3:11<885::AID-ADEM885>3.0.CO;2-P, 2001.

Dyskin, A.V., Estrin, Y., Kanel-Belov, A.J., Pasternak, E., 2003a. Topological interlocking of platonic solids: A way to new materials and structures. Phil. Mag. Lett. 83 (3), 197–203. http://dx.doi.org/10.1080/0950083031000065226, 2003.

Dyskin, A.V., Estrin, Y., Pasternak, E., Khor, H.C., Kanel-Belov, A.J., 2003b. Fracture resistant structures based on topological interlocking with non-planar contacts. Adv. Eng. Mater. 5 (3), 116–119. http://dx.doi.org/10.1002/adem.200390016, 2003.

El-Abbasi, N., Bathe, K.J., 2001. Stability and patch test performance of contact discretizations and a new solution algorithm. Comput. Struct. 79 (16), 1473–1486. http://dx.doi.org/10.1016/S0045-7949(01)00048-7, 2001.

Khandelwal, S., Siegmund, T., Cipra, R., Bolton, J., 2012. Transverse loading of cellular topologically interlocked materials. Int. J. Solids Struct. 49 (18), 2394–2403. http://dx.doi.org/10.1016/j.ijsolstr.2012.04.035, Elsevier Ltd, 2012.

Khandelwal, S., Siegmund, T., Cipra, R.J., Bolton, J.S., 2014. Scaling of the elastic behavior of two-dimensional topologically interlocked materials under transverse loading. J. Appl. Mech. Trans. ASME 81 (3), 1–9. http://dx.doi.org/10.1115/1.4024907, 2014.

Khandelwal, S., Siegmund, T., Cipra, R.J., Bolton, J.S., 2015. Adaptive mechanical properties of topologically interlocking material systems. Smart Mater. Struct. 24 (4), http://dx.doi.org/10.1088/0964-1726/24/4/045037, IOP Publishing.

Konyukhov, A., Schweizerhof, K., 2004. Contact formulation via a velocity description allowing efficiency improvements in frictionless contact analysis. Comput. Mech. 33 (3), 165–173. http://dx.doi.org/10.1007/s00466-003-0515-3, 2004.

Krause, T., Molotnikov, A., Carlesso, M., Rente, J., Rezwan, K., Estrin, Y., Koch, D., 2012. Mechanical properties of topologically interlocked structures with elements produced by freeze gelation of ceramic slurries. Adv. Eng. Mater. 14 (5), 335–341. http://dx.doi.org/10.1002/adem.201100244, 2012.

Laursen, T.A., 2003. Computational Contact and Impact Mechanics. Springer Berlin Heidelberg, Berlin, Heidelberg, http://dx.doi.org/10.1007/978-3-662-04864-1.

Mahoney, K., Siegmund, T., 2022. Mechanics of tubes composed of interlocking building blocks. Internat. J. Engrg. Sci. 174 (February), 103654. http://dx.doi.org/10.1016/j.ijengsci.2022.103654, Elsevier Ltd, 2022.

Mirkhalaf, M., Dastjerdi, A.K., Barthelat, F., 2014. Overcoming the brittleness of glass through bio-inspiration and micro-architecture. Nature Commun. 5, 1–9. http://dx.doi.org/10.1038/ncomms4166, Nature Publishing Group, 2014.

Mirkhalaf, M., Sunesara, A., Ashrafi, B., Barthelat, F., 2019. Toughness by segmentation: Fabrication, testing and micromechanics of architectured ceramic panels for impact applications. Int. J. Solids Struct. 158, 52–65. http://dx.doi.org/10.1016/j.ijsolstr.2018.08.025, Elsevier Ltd, 2019.

Mirkhalaf, M., Zhou, T., Barthelat, F., 2018. Simultaneous improvements of strength and toughness in topologically interlocked ceramics. Proc. Natl. Acad. Sci. USA 115 (37), 9128–9133. http://dx.doi.org/10.1073/pnas.1807272115, 2018.

Schaare, S., Dyskin, A.V., Estrin, Y., Arndt, S., Pasternak, E., Kanel-Belov, A., 2008. Point loading of assemblies of interlocked cube-shaped elements. Internat. J. Engrg. Sci. 46 (12), 1228–1238. http://dx.doi.org/10.1016/j.ijengsci.2008.06.012, Elsevier Ltd, 2008.

Schweizerhof, K., Konyukhov, A., 2005. Covariant description for frictional contact problems. Comput. Mech. 35 (3), 190–213. http://dx.doi.org/10.1007/s00466-004-0616-7, 2005.

Wriggers, P., Krstulovic-Opara, L., Korelc, J., 2001. Smooth C1-interpolations for two-dimensional frictional contact problems. Internat. J. Numer. Methods Engrg. 51 (12), 1469–1495. http://dx.doi.org/10.1002/nme.227, 2001.

Wriggers, P., Laursen, T.A., 2007. Computational Contact MechanicsCISM Courses and Lectures, 498, 498.

Yastrebov, V.A., Breitkopf, P., 2013. Numerical Methods in Contact Mechanics. John Wiley and Sons, Inc., Hoboken, NJ USA, http://dx.doi.org/10.1002/9781118647974.

Zakeri, M., Majidi, M., Haghighi-Yazdi, M., Safarabadi, M., 2021. Numerical analysis of linear and nonlinear buckling instability of plates made of topologically interlocked materials. Mech. Based Des. Struct. Mach. 1–13. http://dx.doi.org/10.1080/15397734.2021.1921596, Taylor and Francis, 2021.

Zavarise, G., De Lorenzis, L., 2009a. A modified node-to-segment algorithm passing the contact patch test. Internat. J. Numer. Methods Engrg. 79 (4), 379–416. http://dx.doi.org/10.1002/nme.2559, 2009.

Zavarise, G., De Lorenzis, L., 2009b. The node-to-segment algorithm for 2D frictionless contact: Classical formulation and special cases. Comput. Methods Appl. Mech. Engrg. 198 (41–44), 3428–3451. http://dx.doi.org/10.1016/j.cma.2009.06.022, Elsevier B.V., 2009.